Fiber Laser Welded AZ31 Magnesium Alloy: The Effect of Welding Speed on Microstructure and Mechanical Properties

S.H. CHOWDHURY, D.L. CHEN, S.D. BHOLE, E. POWIDAJKO, D.C. WECKMAN, and Y. ZHOU

This study was aimed at characterizing microstructural change and evaluating tensile and fatigue properties of fiber laser welded AZ31B-H24 Mg alloy with special attention to the effect of welding speed. Laser welding led to the formation of equiaxed dendrites in the fusion zone and columnar dendrites near the fusion zone boundary along with divorced eutectic $Mg_{17}Al_{12}$ particles and recrystallized grains in the heat-affected zone. The lowest hardness across the weld appeared in the fusion zone. Although the yield strength, ductility, and fatigue life decreased, the hardening capacity increased after laser welding, with a joint efficiency reaching about 90 pct. A higher welding speed resulted in a narrower fusion zone, smaller grain size, higher yield strength, and longer fatigue life, as well as a slightly lower strain-hardening capacity mainly because of the smaller grain sizes. Tensile fracture occurred in the fusion zone, whereas fatigue failure appeared essentially in between the heat-affected zone and the fusion zone. Fatigue cracks initiated from the near-surface welding defects and propagated by the formation of fatigue striations together with secondary cracks.

DOI: 10.1007/s11661-011-1042-z

I. INTRODUCTION

TODAY, decreasing weight in ground vehicles and aircraft is considered one of the most effective approaches to improve fuel economy and reduce anthropogenic environment-damaging emissions.[1–4] The development and application of magnesium (Mg) alloys, being the lightest structural metallic materials, have thus attracted considerable interest in the automotive and aerospace industries in recent years because of their light weight and good mechanical properties.[1,5–8]

The structural applications of Mg alloys inescapably involve an important manufacturing process—welding. Some processing problems and welding defects such as oxide films, crack, and porosity could easily be caused by the physical properties of Mg, such as its strong tendency to oxidize, high thermal conductivity, low melting and boiling temperatures, high solidification shrinkage, and tendency to form low melting point constituents, low viscosity, and high solubility for hydrogen in the liquid state.[9] Weisheit *et al.*[10] performed CO_2 laser welding of different Mg alloys and showed that most Mg alloys can be easily welded without serious defects, except AZ series and AM series, which exhibited extremely high levels of porosity. Zhao and Debroy[11] investigated the formation of porosity in an AM60 Mg alloy during laser welding and concluded that hydrogen in the parent material was the main origin of porosity in the welds. Sun *et al.*[12] evaluated TIG, CO_2, and pulsed Nd:YAG laser welded joints of AZ31 sheet and reported that TIG welding could be used to achieve welds without defects, but noted that coarser grain sizes in TIG welds could diminish the mechanical properties. Recently, among the several types of lasers, attention has been paid to fiber lasers, because this type of laser presents several benefits for industrial applications, namely high power with low beam divergence, flexible beam delivery, low maintenance costs, high efficiency of laser generation, and compact size of laser apparatus.[13] After fiber laser welding (FLW), microstructural changes occurred across the welded joint including local variations of grain sizes in the fusion zone (FZ) and heat-affected zone (HAZ), grain shape and orientation, and formation of porosity. These microstructural changes could affect the mechanical properties such as tensile and fatigue strength, and strain-hardening behavior, as well as potentially compromise the integrity and longevity of the welded joints and structures.

Limited work on the FLW of Mg alloys has recently been reported. Sakai *et al.*[14] conducted welding on a 2-mm-thick extruded sheet of Mg-6Al-2Ca alloy at a welding speed of 10 m/min using a 3-kW fiber laser, and obtained the tensile strength of welded joints reaching about 84 to 88 pct of that of the base metal (BM). Liu *et al.*[15] also performed welding of an ACM522 Mg alloy using a fiber laser and showed that sound welds without major defects could be achieved. However, porosity in the fiber laser welds of two thixomolded Mg

S.H. CHOWDHURY, Graduate Student, D.L. CHEN, Professor and Ryerson Research Chair, and S.D. BHOLE, Professor, are with the Department of Mechanical and Industrial Engineering, Ryerson University, Toronto, ON M5B 2K3, Canada. Contact e-mail: dchen@ryerson.ca E. POWIDAJKO, Graduate Student, D.C. WECKMAN, Professor, and Y. ZHOU, Professor and Canada Research Chair, are with the Department of Mechanical and Mechatronics Engineering, University of Waterloo, Waterloo, ON N2L 3G1, Canada.

Manuscript submitted June 7, 2011.
Article published online January 5, 2012

alloys AE42 and AS41 occurred, and the volume fraction of porosity in the welds decreased with increasing welding speed.[16] Although the microstructural changes and tensile properties have been studied,[14–16] to the authors' knowledge, the durability-related fatigue resistance of fiber laser welded Mg joints was only reported in our recent study,[17] which was limited to a fixed welding speed. It is unclear how the microstructure, tensile properties, and fatigue life would be affected by the welding speed during FLW. The objective of the present study, therefore, was to characterize the microstructural change and evaluate the tensile and fatigue properties of fiber laser welded joints of AZ31B-H24 Mg alloy with particular focus on the effect of welding speed.

II. EXPERIMENTAL PROCEDURE

The BM in the present study was 2-mm-thick commercial AZ31B-H24 Mg alloy sheet, with a nominal composition of 0.2 to 1.0 wt pct Mn, 0.7 to 1.3 wt pct Zn, 2.5 to 3.5 wt pct Al, and the balance Mg. The surfaces of the plates were chemically cleaned with an acetone and methanol rinse before welding to eliminate surface contaminations. Prior to welding, preexisting surface oxides were removed with a stainless steel wire brush, and then the surface was cleaned using ethanol. Butt welding was conducted without filler metal (Figure 1), using a fiber laser operating at a laser power of 2 kW and two welding speeds of 50 mm/s and 100 mm/s. Using these conditions, keyhole-mode welds were produced in which the laser melted a keyhole in the material being welded because of the higher energy density delivered to the material. As the beam moved forward, the molten metal filled in behind the beam to form the joint.

To examine the microstructure of FZ and HAZ, the welded joints perpendicular to the welding direction were cut, cold mounted, ground, polished, and etched using etchant 1 with water (10 mL acetic acid [99 pct], 4.2 g picric acid, 10 mL H_2O, and 70 mL ethanol [95 pct]) and etchant 2 without water (10 mL acetic acid [99 pct], 4.2 g picric acid, and 70 mL ethanol [95 pct]).[17,18] The microstructure was observed with an optical microscope equipped with quantitative image analysis software. The phases in the FZ, HAZ, and BM were identified using a Panalytical X-ray diffractometer (XRD) via microdiffraction with an incident beam of 300 μm in diameter using CuK_α radiation (wavelength $\lambda = 0.15406$ nm) at 45 kV and 40 mA. The diffraction angle (2θ) at which the X-rays hit the sample varied from 20 deg to 110 deg with a step size of 0.2 deg and 10 seconds in each step. Vickers microhardness was measured with a computerized Buehler microhardness tester across the sectioned weld. A load of 100 g and dwell time of 15 seconds were applied during the microhardness tests. All indentations were adequately spaced to avoid any potential effect of strain fields caused by adjacent indentations.

Subsized tensile specimens in accordance with ASTM standard E8M-08[19] were machined along the rolling (or longitudinal) direction for both welded joints, where the weld was located at the center of the gauge area. Tensile tests were conducted using a fully computerized universal tensile testing machine at constant strain rates of 1×10^{-2} s^{-1}, 1×10^{-3} s^{-1}, 1×10^{-4} s^{-1}, and 1×10^{-5} s^{-1} and at room temperature. At least two samples were tested at each strain rate. An extensometer with a gauge length of 25 mm was used to measure the strain during the tensile tests. Fatigue tests were performed using a fully computerized Instron 8801 servohydraulic testing system under load control at different stress amplitudes. A stress ratio of R ($\sigma_{min}/\sigma_{max}$) equal to 0.1, a sinusoidal waveform, and a frequency of 50 Hz were applied in all the tests. At least two samples were tested at each stress level. The fracture surfaces of fiber laser welded joints after the tensile and fatigue tests were examined via a JSM-6380LV scanning electron microscope (SEM) equipped with an Oxford energy-dispersive X-ray spectroscopy (EDS) system and three-dimensional (3D) fractographic analysis capacity.

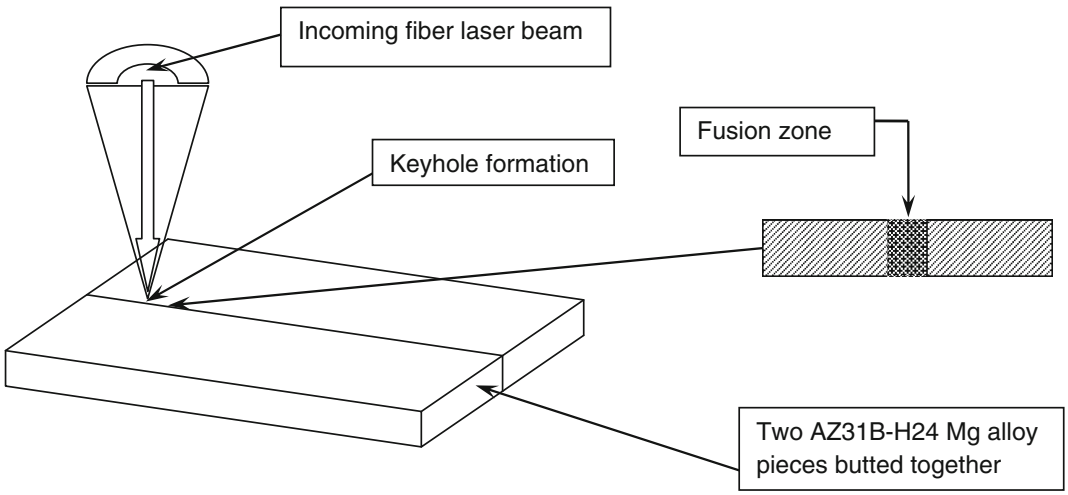

Fig. 1—Schematic illustration of FLW.

III. RESULTS AND DISCUSSION

A. *Microstructure*

Typical microstructures of AZ31B-H24 Mg alloy BM and FLW joints are shown in Figure 2 for a welding speed of 50 mm/s and in Figure 3 for a welding speed of 100 mm/s, respectively. As shown in Figure 2(a), elongated and pancake-shaped grains with varying sizes were observed in the BM. The heterogeneity in the grain structure of the BM was caused by both deformation of the 2-mm-thick sheet by rolling and incomplete dynamic recrystallization (partial annealing). A similar result has been reported for AZ31B-H24 Mg alloy in Reference 20. Laser welding led to a considerable change in the microstructure. Because of the high-power density in FLW that led to a deep and narrow FZ, the weld bead was fairly narrow at both the top and the bottom, and no distortion or drop-through was observed across the weld (Figure 2(b)). However, the lower welding speed of 50 mm/s resulted in a slightly wider FZ (Figure 2(b)), in comparison with that of the welded joint made at a welding speed of 100 mm/s (Figure 3(a)). This was caused by the higher energy input at the lower welding speed. The FZ exhibited typical equiaxed dendritic structures in both welding conditions, containing numerous divorced eutectic β-$Mg_{17}Al_{12}$ precipitates existing basically in the interdendritic and intergranular regions (Figure 2(c) and Figure 3(b)). Such divorced eutectic β-$Mg_{17}Al_{12}$ precipitates only appeared in the FZ, as revealed by the XRD microdiffraction (Figure 4). The presence of the eutectic structure was a result of the nonequilibrium rapid cooling of the weld pool during

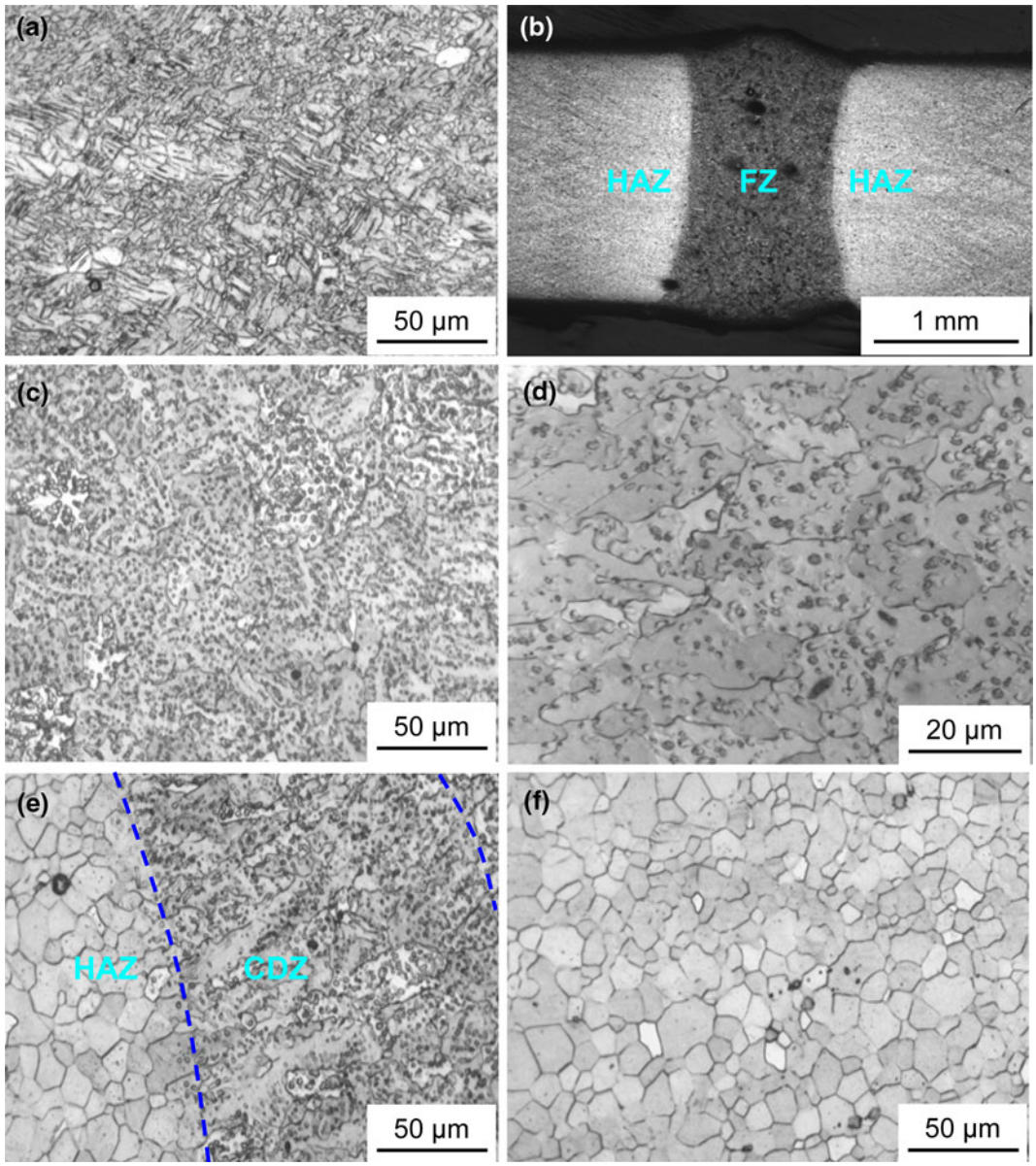

Fig. 2—Typical microstructures of a FLW joint made at a welding speed of 50 mm/s. (*a*) BM AZ31-H24, (*b*) cross section of the welded joint, (*c*) FZ, (*d*) FZ at a higher magnification, (*e*) columnar dendrites near the boundary of fusion zone, (*f*) recrystallized HAZ.

welding. Such β-$Mg_{17}Al_{12}$ precipitates were also observed in the FZ of diode laser,[17] laser/arc hybrid,[21] double-sided arc,[22] and resistance spot welded[23] Mg joints. However, the grain size (or dendrite cell size) in the FZ seemed larger at a lower welding speed of 50 mm/s (Figure 2(c)) than at a higher welding speed of 100 mm/s (Figure 3(b)). As the FLW joint at a welding speed of 50 mm/s had more heat energy deposited in the welding area and a lower cooling rate, the temperature in the FZ would be expected to be higher.[24] This would result in larger sizes of equiaxed dendrite cells along with relatively fewer divorced eutectic β-$Mg_{17}Al_{12}$ precipitates formed in the FZ compared with the FLW joint at a welding speed of 100 mm/s, as shown in Figure 2(d) and Figure 3(c) taken at a higher magnification. A similar effect of welding speed on the dendrite cell sizes in the FZ in a CO_2 laser welded AZ31 magnesium alloy joint was reported in Reference 25 as well. It was reported that the higher the casting temperature (or pouring temperature during casting), the larger the dendrite cell/grain size and the secondary dendrite arm spacing for aluminum alloys[26,27] and a superalloy.[28] Gilath *et al.*[29] proposed the following expression:

$$d = \frac{C}{\sqrt{v}} \qquad [1]$$

where d is the dendrite spacing, v is the welding speed, and C is an empirical constant. Based on Eq. [1], a larger dendrite cell/grain size should be observed in the FZ at a lower welding speed of 50 mm/s.Near the fusion boundary, columnar dendrites formed in both welded joints (Figures 2(e) and 3(d)). The width of the columnar dendrite zone (CDZ) increased with decreasing welding speed from 100 mm/s to 50 mm/s (Figures 2(e) and 3(d)), respectively. Similar results have been reported in Reference 30. The formation of columnar dendrites was caused by the presence of a larger

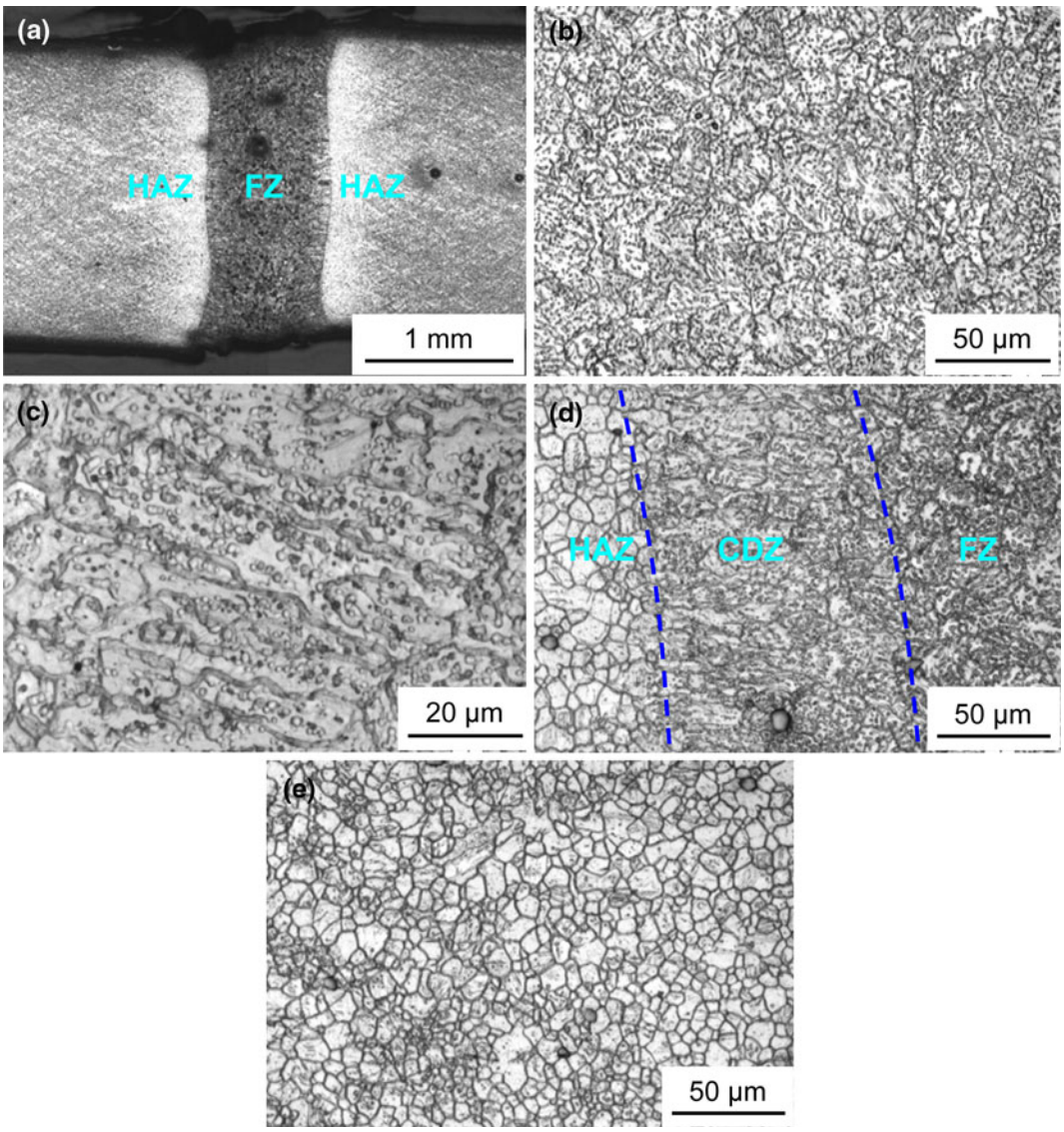

Fig. 3—Typical microstructures of a FLW joint made at a welding speed of 100 mm/s. (*a*) cross section of the welded joint, (*b*) dendrites in the FZ, (*c*) FZ at a higher magnification, (*d*) columnar dendrites near the boundary of fusion zone, (*e*) recrystallized HAZ.

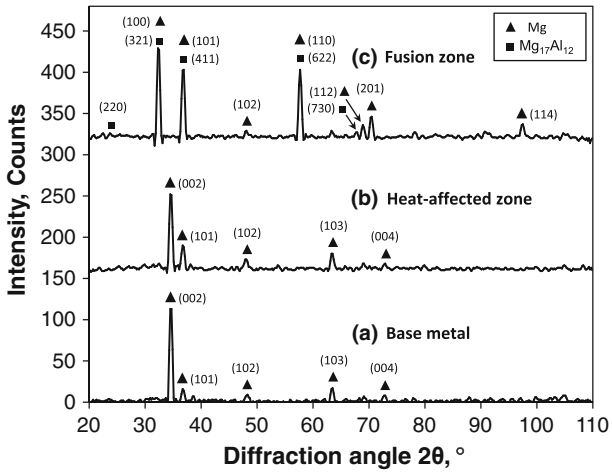

Fig. 4—X-ray diffraction patterns obtained from (*a*) BM, (*b*) HAZ, and (*c*) FZ of a FLW joint made at a welding speed of 50 mm/s.

temperature gradient near the fusion boundary than in the weld pool center, as reported by Kou.[31] In the HAZ, the originally elongated and partially deformed BM structure had become equiaxed grains in both welded joints (Figures 2(f) and 3(e)), suggesting that recrystallization and grain growth occurred in the HAZ where no divorced eutectic β-$Mg_{17}Al_{12}$ precipitates were present in contrast to the FZ microstructure. This is also visible from the XRD microdiffraction spectra shown in Figure 4. It is clear that the size of grains in the HAZ was larger at a slower welding speed of 50 mm/s (Figure 2(f)) than at a faster welding speed of 100 mm/s (Figure 3(e)). Again, this was attributed to the higher energy input leading to a higher temperature in the HAZ, which sustained a longer time at the slower welding speed.

It should be noted that some small pores were observed in the FZ, which is more visible on the fracture surface in the later section. Some particles were also observed in the FLW joints (Figure 5(a)). EDS analysis revealed that these particles were unmelted Mn- and Al-containing inclusions (Figure 5(b)), which were still present in the weld pool. These particles could act as nuclei and block off the epitaxial columnar dendrite grains. Similar results were also reported by Xiao *et al.*,[32] where they observed that more unmelted Mn-Al particles resulted in a more efficient nucleation, resulting in a finer grain size in the FZ of the weld. Again, several divorced eutectic β-$Mg_{17}Al_{12}$ precipitates were visible nearly uniformly in FZ in conjunction with Mn-Al particles (Figure 5(a)).

B. *Microhardness Profile*

Figure 6 shows a typical hardness profile along the midthickness of the 2-mm-thick FLW AZ31B-H24 Mg joints that were welded at a welding speed of 50 mm/s and 100 mm/s with 2-kW laser power. The lowest hardness appeared at the center of the FZ after laser welding. The hardness value decreased gradually from about 73 HV of the BM in the half-hardened H24 temper to approximately 54 HV at the center of the FZ across the HAZ for the welding speed of 100 mm/s, and to about 51 HV for the welding speed of 50 mm/s. The

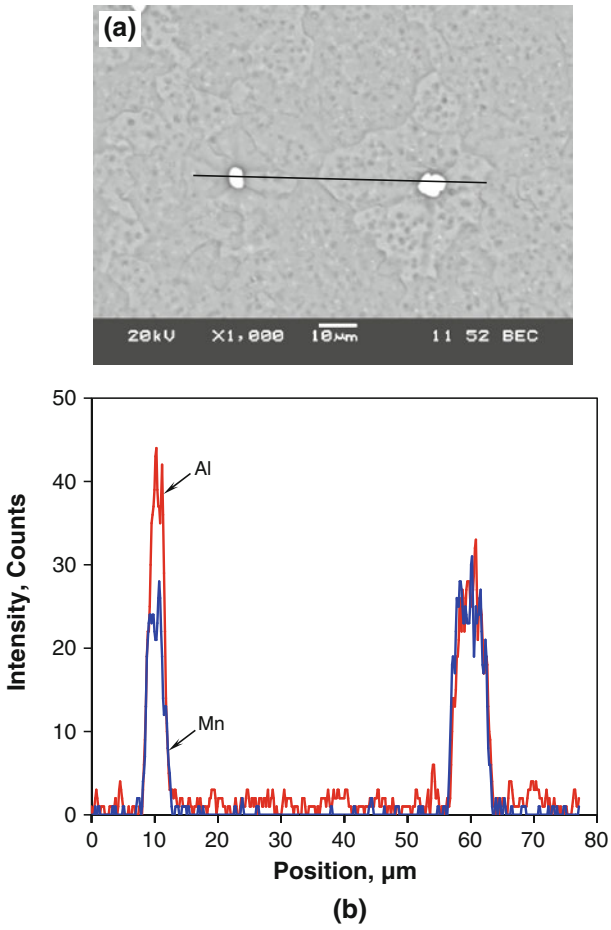

Fig. 5—(*a*) SEM micrograph of particles in the FZ of FLW joint made at a welding speed of 50 mm/s, (*b*) EDS line scan across the two particles in (a) showing Al and Mn compositional variations across the particles in the FZ.

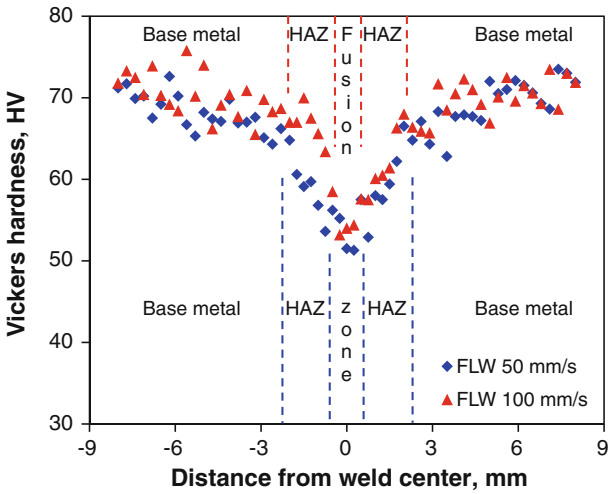

Fig. 6—Typical microhardness profile of FLW butt joints at a welding speed of 50 mm/s and 100 mm/s.

hardness of the FLW joint made at a welding speed of 100 mm/s was generally higher than that made at a welding speed of 50 mm/s, with the lowest hardness in the FZ varying from 70 pct to 74 pct of the BM when the welding speed increased from 50 to 100 mm/s. This finding is a result of the larger sizes of equiaxed dendrite grains formed in the FZ (Figures 2(c) *vs* 3(b)) and larger grain sizes in the HAZ (Figures 2(f) *vs* 3(e)) at the lower welding speed. A strong grain size dependence of microhardness was observed, following the Hall–Petch type relationship in the welded AZ31B-H24 Mg alloy.[20] Because the grain boundaries were the main obstacle to the slip of dislocations, the material with a smaller grain size would have a stronger resistance to the localized plastic deformation as a result of the presence of more grain boundaries, giving rise to a higher hardness or strength. Another reason for the higher hardness would be related to the formation of finer dendrite arm spacing at a higher welding speed, as reported by Turhal and Kan.[33] The overall reduction in hardness after laser welding, shown in Figure 6, is attributed to the changes in the microstructure from the deformed and elongated grains in the BM in the half-hardened and partially annealed H24 state (Figure 2(a)) to the nonequilibrium dendritic solidification structure (Figures 2(c) and 3(b)) in conjunction with divorced eutectic β-$Mg_{17}Al_{12}$ particles in the FZ (Figures 2(d), 3(c), and 4), as well as the recrystallized equiaxed grains in the HAZ (Figures 2(f) and 3(e)). Because of the narrower FZ and HAZ, the hardness profile at a welding speed of 100 mm/s appeared sharper, as shown in Figure 6.

C. *Tensile Properties*

Figure 7 shows typical stress–strain curves for the BM, FLW AZ31B-H24 Mg alloy joints made at different welding speeds of 50 mm/s and 100 mm/s and tested at a strain rate of 1×10^{-4} s^{-1}. After welding, both the strength and the elongation (pct El) decreased. More reduction in the yield strength (YS) and ultimate tensile strength (UTS) occurred in the FLW joint at the welding speed of 50 mm/s than at 100 mm/s. This finding was caused by the larger dendrite cells/grains in the FZ (Figure 2(c)) and equiaxed recrystallized grains in the HAZ (Figure 2(f)) at the slower welding speed. As mentioned earlier, the weld exhibited a typical dendritic solidification structure containing numerous brittle divorced eutectic β-$Mg_{17}Al_{12}$ particles (Figures 2(d) and 3(c)), which was significantly different from the microstructure of the rolled and partially annealed BM (Figure 2(a)). All of the FLW joints fractured in the FZ during the tensile tests, corresponding to the lowest hardness there (Figure 6). As a result, the ductility of the AZ31B-H24 Mg alloy after laser welding diminished.

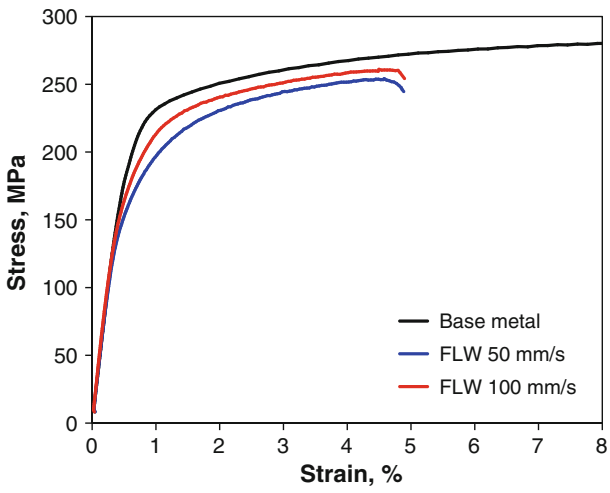

Fig. 7—Typical engineering stress–strain curves of the AZ31B-H24 Mg base alloy, FLW joints made at a welding speed of 50 mm/s and 100 mm/s, tested at a strain rate of 1×10^{-4} s^{-1}.

The evaluated YS, UTS, and percent elongation of the BM and FLW AZ31B-H24 Mg alloy joints are plotted in Figure 8. At all strain rates, both the YS and the UTS became lower after laser welding. Although the welding led to a relatively larger decrease in the YS, the reduction of the UTS was moderate with a joint efficiency of about 89 pct at a welding speed of 50 mm/s and about 91 pct at a welding speed of 100 mm/s. Some values of joint efficiency for different Mg alloys are summarized in Table I, where the joint efficiency is the ratio of the UTS of welded joints to the UTS of the corresponding base alloy.

A wide range of joint efficiency between ~59 pct and 97 pct could be obtained, which was associated with the welding processes and parameters as well as the initial state (or initial strength) of the material. The joint efficiency of the 2-mm-thick AZ31B-H24 Mg alloy achieved in the present study using a 2-kW fiber laser at a welding speed of either 50 mm/s or 100 mm/s was higher than that of about 84~88 pct for the same thickness extruded sheet of Mg-6Al-2Ca alloy using a 3-kW fiber laser at a welding speed of 67 mm/s to 167 mm/s.[14] As the strain rate increased from 1×10^{-5} s^{-1} to 1×10^{-2} s^{-1}, the YS and UTS of the BM increased to a certain degree but the ductility decreased considerably. This observation indicated the presence of a stronger strain rate sensitivity in the BM because of the smaller grain size (Figure 2(a)). Similar results for the effect of grain size on the strain rate sensitivity were also reported in an extruded AZ31 Mg alloy.[37] As dislocations tend to pile up at grain boundaries during deformation, the smaller grains with more grain boundaries would facilitate the dislocation pile ups. del Valle and Ruano[38] reported the following relationship between the strain rate sensitivity $(\partial\sigma/\partial \ln \dot{\varepsilon})$ and grain size (d) as follows:

$$\frac{\partial \sigma}{\partial \ln \dot{\varepsilon}} = \frac{k}{2} d^{-1/2}\left(M_c - 2M_{cg}\right) + \sigma M_{cg} \qquad [2]$$

where σ is flow stress, $\dot{\varepsilon}$ is strain rate, k is Boltzmann's constant, and M_{cg} $(\partial \ln \sigma_{cg}/\partial \ln \dot{\varepsilon})$ and M_c $(\partial \ln \tau_c/\partial \ln \dot{\varepsilon})$ can be treated as constants.[37,38] This equation expresses a linear relationship between the strain rate sensitivity and the grain size in the form of $d^{-1/2}$, similar to the well-known Hall–Petch equation. It follows that the strain rate sensitivity increases with decreasing grain size. Because the grain size in the AZ31B-H24 BM was

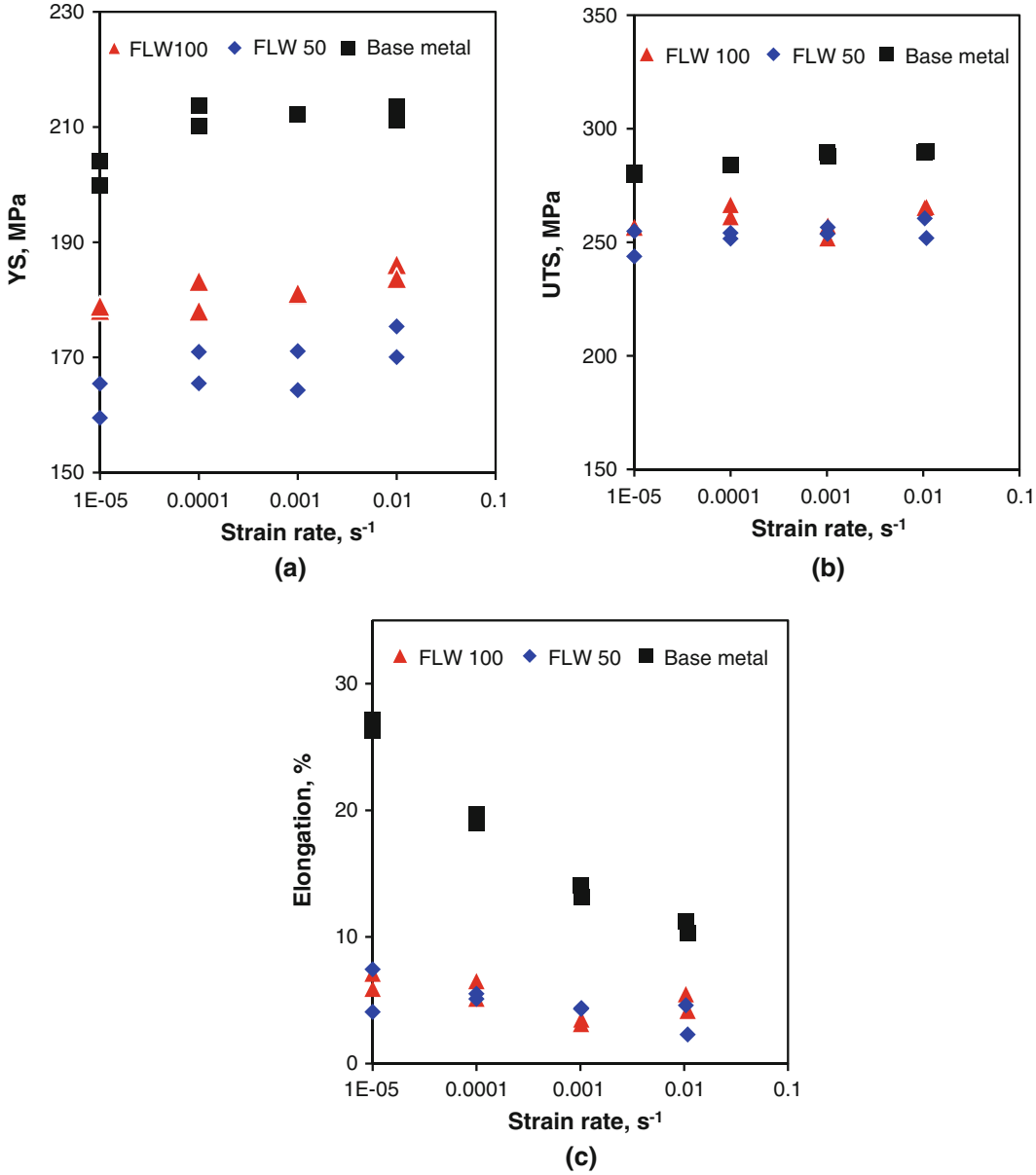

Fig. 8—Effect of strain rate on (*a*) YS, (*b*) UTS, and (*c*) ductility of the AZ31B-H24 BM, FLW joints made at a welding speed of 50 mm/s and 100 mm/s.

smaller (Figure 2(a)), the strain rate sensitivity would be higher, as shown in Figure 8. After laser welding, the strain rate sensitivity became relatively weaker, as demonstrated by the small increase in YS and UTS and the slight decrease in the ductility with increasing strain rate (Figure 8). Another reason for the reduction in the tensile properties after welding is related to the formation of a new crystallographic texture in the weld zone as reported by Park *et al.*[39] Future study of the texture change after laser welding is needed.

D. *Strain-Hardening Behavior*

The FLW was anticipated to affect the strain- (or work-) hardening characteristics of AZ31B-H24 Mg alloy as well. The hardening capacity of a material, H_c, has been defined as a normalized parameter as follows[40]:

$$H_c = \frac{\sigma_{\mathrm{UTS}} - \sigma_{\mathrm{y}}}{\sigma_{\mathrm{y}}} = \frac{\sigma_{\mathrm{UTS}}}{\sigma_{\mathrm{y}}} - 1 \qquad [3]$$

where $\sigma_{\mathrm{y}}$is the yield strength, and σ_{UTS} is the ultimate tensile strength of a material. The obtained hardening capacity of the BM and the FLW samples is listed in Table II.The hardening capacity increased after FLW, especially for the FLW samples at a lower welding speed of 50 mm/s. Strain rate had little effect on the hardening capacity. A decrease in the grain size would increase the YS as indicated by the Hall–Petch relationship[41] because it reduced the difference in flow resistance between the grain boundary and the interior, which in turn lowered the hardening capacity.[42] Because the grain size of the FLW

Table I. Joint Efficiency for the Welded Joints of Different Mg Alloys

Material Condition	Welding Process	BM		Welding Parameter	Welded Joint		Joint Efficiency, pct	Ref.
		YS (MPa)	UTS (MPa)		YS (MPa)	UTS (MPa)		
AMC602 extruded sheet	FLW	—	250	3000 W- 66.67~166.67 mm/s	—	209~220	84~88	14
AZ31-H24	Diode laser welding	209	285	3000 W-8.33 mm/s	91	169	59	17
AZ31-H24	Friction stir welding	208	309	1000 rpm-4 mm/s	—	201	65	20
AZ31-H24	Double-sided arc welding	209	285	1400 W-25 mm/s	128	236	83	22
	Friction stir welding	209	285	1000~2000 rpm 10~30 mm/s	120~161	212~239	74~84	
AZ31 wrought	CO_2 laser welding	—	315	800~1000 W 25~41.66 mm/s		205~305	65~96	30
AZ31-H24	Friction stir welding	227.6	307.7	1500~2000 rpm 1.3~3.4 mm/s	94.9~115.3	200~225.6	65~73	34
AM50	Friction stir welding	117	260	—	110	224	86	35
AZ31B	Gas tungsten arc welding	171	215	3 mm/s	148	183	85	36
	Friction stir welding			1600 rpm -0.66 mm/s	171	208	95	
	CO_2 laser welding			2500 W-91.66 mm/s	174	212	97	

samples at a welding speed of 50 mm/s (Figures 2(c) and 2(f)) was larger than that of the FLW samples at a welding speed of 100 mm/s (Figures 3(b) and 3(e)), a higher value of hardening capacity in the FLW samples at a welding speed of 50 mm/s is expected.

Another way of understanding the strain-hardening behavior is to determine the strain-hardening exponent, because it is a measure of the ability of a material to strain harden; the larger its value, the greater the strain hardening for a given amount of plastic strain. A few equations have been proposed to evaluate the strain-hardening exponent. Hollomon[43] proposed the following expression:

$$\sigma = K\varepsilon^n \qquad [4]$$

where n is the strain-hardening exponent, K is the strength coefficient, σ is the true stress, and ε is the true strain. To better quantify the strain-hardening response, Chen and Lu[44] fit their tensile curves using the Ludwik equation[45]:

$$\sigma = \sigma_y + K_1\varepsilon^{n1}, \qquad [5]$$

where n_1 is the strain-hardening exponent, and K_1 is the strength coefficient, which represents the increment in strength caused by strain hardening at $\varepsilon = 1$. Afrin *et al.*[40] proposed the following equation by considering only the net flow stress and net plastic strain of a material after yielding:

$$\sigma = \sigma_y + K^*\left(\varepsilon - \varepsilon_y\right)^{n^*} \qquad [6]$$

where n^*, σ, ε, σ_y, and ε_y are the strain-hardening exponent, true stress, true strain, YS, and yield strain of a material, respectively. K^* is the strength coefficient, which reflects the increment in strength caused by strain hardening corresponding to $(\varepsilon - \varepsilon_y) = 1$. The strain-hardening exponents evaluated according to the previous three equations are shown in Figures 9(a) through (c) for the BM and FLW joints made at a welding speed of 50 mm/s and 100 mm/s as a function of strain rate. Only the data lying in between the YS and UTS were used to evaluate the value of n, n_1, and n^*. Almost no effect of strain rate on the strain-hardening exponents was observed in the BM. But for the FLW samples, the strain-hardening exponents increased with increasing strain rate. It is also shown that the n values were the smallest and n_1 values were the highest with n^* lying between the two values. The strain-hardening exponents evaluated corresponding to the previous three equations were obviously higher after welding, and the FLW joints made at 50 mm/s exhibited higher strain-hardening exponents than the FLW joints made at 100 mm/s, as shown in Figure 9.

One important contribution to strain hardening is associated with the formation and multiplication of dislocations. In the plastic deformation stage, the net flow stress in relation to the dislocation density could be expressed as follows[40,46,47]:

$$\sigma - \sigma_y \propto \sqrt{\rho} \qquad [7]$$

where ρ is the dislocation density. The net flow stress necessary to continue deformation of a material is

Table II. YS, UTS, Hardening Capacity, and Strain-Hardening Exponents of the BM and FLW Samples of AZ31B-H24 Mg Alloy Tested at Different Strain Rates

Specimen	Welding Speed (mm/s)	Strain Rate (s^{-1})	YS (MPa)	UTS (MPa)	Hardening Capacity	n-Value	n_1- Value	n*-Value
Base metal	—	1×10^{-2}	212	289	0.37	0.113	0.371	0.368
		1×10^{-3}	212	288	0.36	0.117	0.387	0.347
		1×10^{-4}	211	283	0.36	0.111	0.392	0.358
		1×10^{-5}	201	280	0.41	0.118	0.395	0.357
Fiber laser welding	50	1×10^{-2}	172	256	0.48	0.229	1.306	0.646
		1×10^{-3}	167	255	0.52	0.229	1.223	0.624
		1×10^{-4}	168	252	0.50	0.214	1.407	0.760
		1×10^{-5}	162	249	0.54	0.208	1.073	0.581
Fiber laser welding	100	1×10^{-2}	184	265	0.43	0.234	1.196	0.584
		1×10^{-3}	181	254	0.41	0.221	1.411	0.627
		1×10^{-4}	180	263	0.46	0.181	0.997	0.548
		1×10^{-5}	178	256	0.44	0.174	0.988	0.544

proportional to the square root of the dislocation density. The dislocation density in a metal increased with the amount of deformation or cold work resulting from dislocation multiplication or the formation of new dislocations, which in turn decreased the spacing among dislocations and their interactions became repulsive. The net result would be that the movement of a dislocation was blocked by other dislocations. As the dislocation density increased, the resistance to dislocation movement by other dislocations became more pronounced. Then a higher stress was necessary to deform the material.[41]

Figure 10 shows a typical Kocks–Mecking plot of the strain-hardening rate ($\theta = d\sigma/d\varepsilon$) *vs* net flow stress ($\sigma - \sigma_y$) in the BM, FLW samples at a welding speed of 50 mm/s and 100 mm/s tested at a strain rate of 1×10^{-5} s^{-1}. Stage III hardening occurred after yielding followed by stage IV hardening for both the BM and the FLW joints. The strain hardening could be understood as a result of the grain size strengthening and dislocation strain hardening, as shown in the following equation[40,46,47]:

$$\sigma = \sigma_o + \sigma_{HP} + \sigma_d \quad [8]$$

where σ_o is the frictional contribution, $\sigma_{HP} = kd^{-1/2}$ is the Hall-Petch contribution, and $\sigma_d = M\alpha Gb\rho^{1/2}$ is the Taylor dislocation contribution (where G is the shear modulus, b is the Burgers vector, M is the Taylor factor, and α is a constant). Sinclair *et al.*[48] and Kovacs *et al.*[49] reported that at lower strains the grain size had a strong contribution to the strain hardening and that the influence of the grain size on the strain hardening decreased at higher strains as a result of dislocation screening and dynamic recovery effects at grain boundaries. Because the BM had a smaller grain size (Figure 2(a)), the Hall–Petch contribution (σ_{HP}) would be stronger at lower strains, leading to a somewhat higher initial strain-hardening rate in comparison with the welded joints. Similar results were reported by Balik *et al.*[50] Figure 10 also shows that the steepness (or slope) of stage III decreased from the BM to the FLW joint at 100 mm/s and to that at 50 mm/s, implying that the decrease in the strain-hardening rate with increasing net flow stress was more enduring.

E. *Fatigue Strength*

Figure 11(a) shows S-N curves obtained at R = 0.1, 50 Hz, and room temperature for the AZ31B-H24 BM FLW joints made at a welding speed of 50 mm/s and 100 mm/s. Similar to the tensile properties (Figure 8), the fatigue life decreased after laser welding, and the fatigue life of the FLW joints made at a welding speed of 100 mm/s was basically longer than that of the FLW joints made at a welding speed of 50 mm/s. The obtained fatigue limit (*i.e.*, the fatigue strength at 1×10^7 cycles) and fatigue ratio (the ratio of fatigue limit to UTS) of the BM and FLW joints are listed in Table III.

The fatigue limit of the FLW samples at a welding speed of 50 mm/s and 100 mm/s dropped by about 40 pct, and the fatigue ratio for both FLW joints decreased by about 32 pct and 35 pct relative to that of the BM. This indicates that the welded joints were more susceptible to the dynamic fatigue loading than quasi-static tensile loading (Table II) where both the YS and the UTS exhibited only a moderate reduction after FLW. Again, the decrease in the fatigue resistance after welding was mainly attributed to the microstructural change, as illustrated in Figures 2 and 3. The following Basquin-type equation[51] can be used to fit the obtained fatigue data:

$$\sigma_\alpha = \sigma'_f(2N_f)^b \quad [9]$$

where σ_a is the cyclic stress amplitude, σ'_f is the fatigue strength coefficient defined by the stress intercept at $2N_f = 1$, N_f is the number of cycles to failure, $2N_f$ is the number of reversals to failure, and b is the fatigue strength exponent, which varying normally between –0.05 and –0.12 for most of the metals is a predominant factor for estimating the fatigue life of materials. Based on Eq. [9], a smaller value of b (in the absolute value) corresponds to a longer fatigue life. Figure 11(b) shows that Eq. [9] could be used to characterize the fatigue data obtained in the present study. It should be noted that the run-out data for which no failure occurred at or over 1×10^7 cycles were not included in the fitting. The obtained b and σ'_f values are listed in Table III. It is shown that the absolute value of fatigue strength

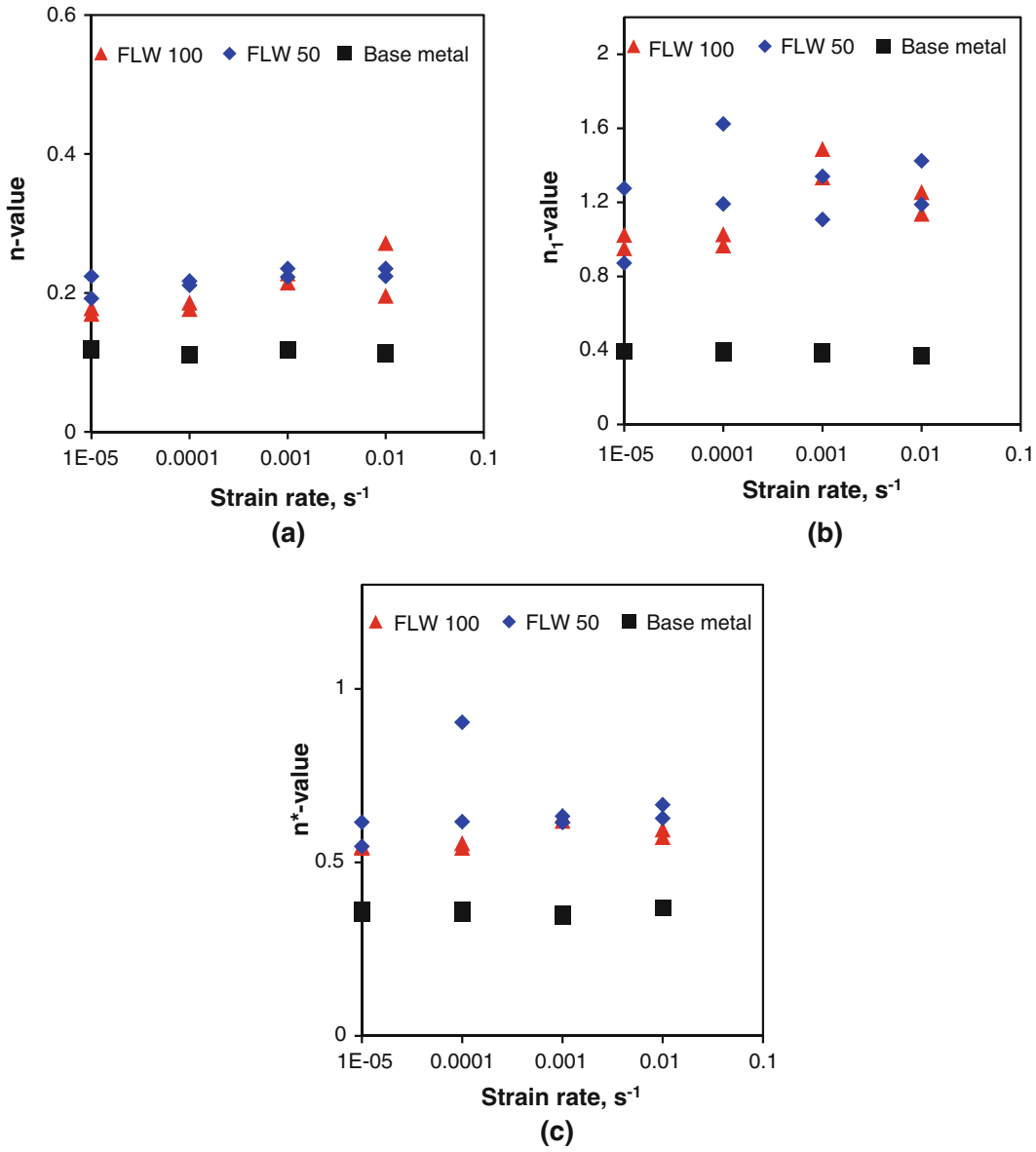

Fig. 9—Effect of strain rate on the strain-hardening exponent (*a*) *n*-value, (*b*) n_1, and (*c*) *n**-value of the AZ31B-H24 BM FLW joints made at a welding speed of 50 mm/s and 100 mm/s.

exponent, *b* was in the following sequence: BM < FLW joints made at a welding speed of 100 mm/s < FLW joints made at a welding speed of 50 mm/s. This finding corresponded well to the longer fatigue life for the BM and shorter fatigue life for the FLW joints made at a welding speed of 50 mm/s, whereas the FLW joints made at a welding speed of 100 mm/s were between them, as shown in Figures 11(a) and (b). The longer fatigue life observed in the FLW samples at a higher welding speed of 100 mm/s was mainly caused by the smaller grain sizes in both FZ (Figure 3(b) *vs* 2(c)) and HAZ (Figure 3(e) *vs* 2(f)), in conjunction with the presence of divorced eutectic β-$Mg_{17}Al_{12}$ particles in the FZ. This outcome was consistent with the higher hardness across the weld (Figure 6) and tensile strength (Figure 8) in the welded joint made at a higher welding speed. Similar results were also obtained by Padmanaban and Balasubramanian,[52] where the superior fatigue properties of AZ31 magnesium welded joints made using a 2.5-kW CO_2 laser were associated with the formation of smaller grains in the weld region, higher FZ hardness, and uniformly distributed finer precipitates.

F. *Fractography*

Tensile fracture usually occurred from the welding pores or defects in the FZ, corresponding well to the lowest hardness shown in Figure 6. Figure 12 shows typical SEM images of the tensile fracture surfaces of the FLW joints at welding speeds of 50 mm/s and 100 mm/s tested at a strain rate of 1×10^{-4} s^{-1}. The tensile fracture surface characteristics were similar at both welding speeds. Several small pores, believed to

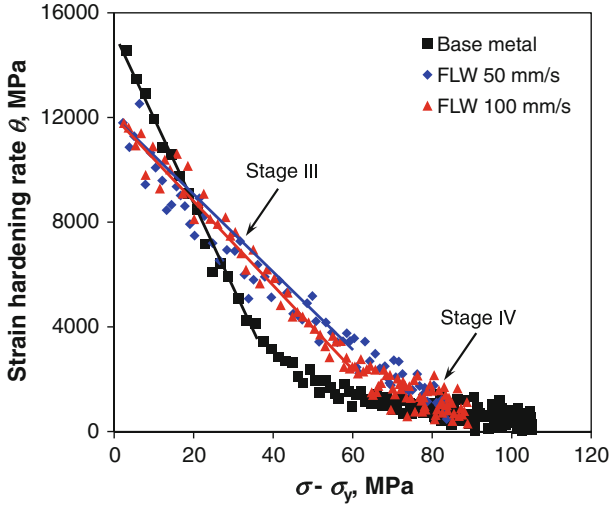

Fig. 10—Strain-hardening rate (θ) as a function of net flow stress ($\sigma - \sigma_y$) of the base alloy, FLW samples at a welding speed of 50 mm/s and 100 mm/s tested at a strain rate of 1×10^{-5} s^{-1}.

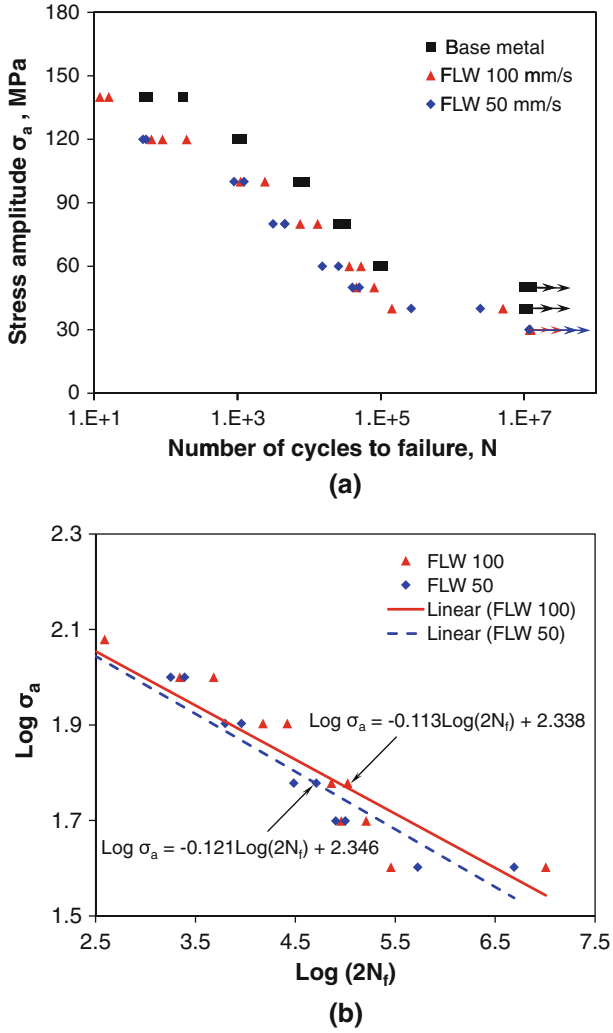

Fig. 11—S-N curves of the AZ31B-H24 BM and FLW joints made at a welding speed of 50 mm/s and 100 mm/s tested at R = 0.1, 50 Hz, and room temperature. (*a*) Stress amplitude (σ_a) *vs* the number of cycles to failure (N_f) in the semilog scale, and (*b*) stress amplitude (σ_a) *vs* the number of reversals to failure ($2N_f$) in the double-log scale.

stem from the air or hydrogen trapped at the solidifying front in the FZ during keyhole FLW, were evident as indicated by arrows in Figures 12(a) and (c), leading to the decreased tensile and fatigue strength, especially ductility (pct El) after welding (Figures 8 and 11). Some ductile tear ridges together with some cleavage-like brittle fracture characteristics appeared on both fracture surfaces of the welded samples as shown in Figures 12(b) and (d). The fractographic observations corresponded well to the relatively low ductility of ~4 pct elongation in the FLW samples (Figure 8(c)).

Figures 13 and 14 show SEM images of fatigue fracture surfaces of the FLW joints made at a welding speed of 50 mm/s and 100 mm/s, respectively. Fatigue cracking essentially initiated from the welding defects at or near the surface (Figures 13(a) through (c) and 14(a) through (c)), irrespective of the applied cyclic stress level. Such welding defects were considered to form because of a marginal incision or depression of molten pool during solidification,[53] or other processing issues such as spatter, sag, undercut, unstable weld pool, liquation and solidification cracking, unstable weld pool, oxide inclusions, and loss of alloying elements.[9] At both welding speeds, welding defects and small pores were observed (Figures 13(b), (c), and (e) and 14(b), (c), and (e)). Yu *et al.*[54] suggested that the formation of the small pores was closely related to the stability of the keyhole and the oscillation of the molten pool during the FLW. The tip of the keyhole was small enough that it could be readily closed by the flow of molten metal and formed as a bubble. A bubble usually became a gas cavity in the weld bead because it was often difficult for bubbles to escape from the molten pool at high solidification rates of laser welding as a result of the fast cooling.[54]

At both welding speeds, single crack initiation basically occurred from the surface defect, and failure occurred perpendicular to the loading direction at lower stress amplitudes (Figure 13(a), the lower sample in Figure 13(f), and Figure 14(a)), whereas multiple crack initiation sites were more obvious at higher stress amplitudes as shown in Figures 13(b) and 14(b) when fracture occurred mainly at ~45 deg shear to the loading direction (the upper sample in Figure 13(f)). Even without surface welding defects, surface grains were usually less constrained than the internal grains; thus, the occurrence of slip in a few grains near the specimen surface became relatively easier during fatigue.[55]

Fatigue crack propagation was mainly characterized by fatigue striations (Figures 13(d) and 14(d)) along with secondary cracks, which appeared usually perpendicular to the fatigue crack propagation direction. The fatigue striations normally occurred by a repeated plastic blunting-sharpening process in the face-centered cubic materials because of the slip of dislocations in the plastic zone ahead of the fatigue crack tip.[56] The formation of fatigue striations in the magnesium alloys

Table III. Fatigue Limit, Fatigue Ratio, Fatigue Strength Coefficient σ_f' and Fatigue Strength Exponent b of the BM and FLW Joints of the AZ31B-H24 Mg Alloy Tested at R = 0.1, 50 Hz, and Room Temperature*

Specimen	Welding Speed (mm/s)	Fatigue Limit (MPa)	Fatigue Ratio	σ_f' (MPa)	b
Base metal	—	50	0.173	246	–0.105
Fiber laser welding	50	30	0.117	222	–0.121
Fiber laser welding	100	30	0.115	218	–0.113

*More test data for the welding speed of 100 mm/s are included in the fitting in comparison with our earlier publication.[17]

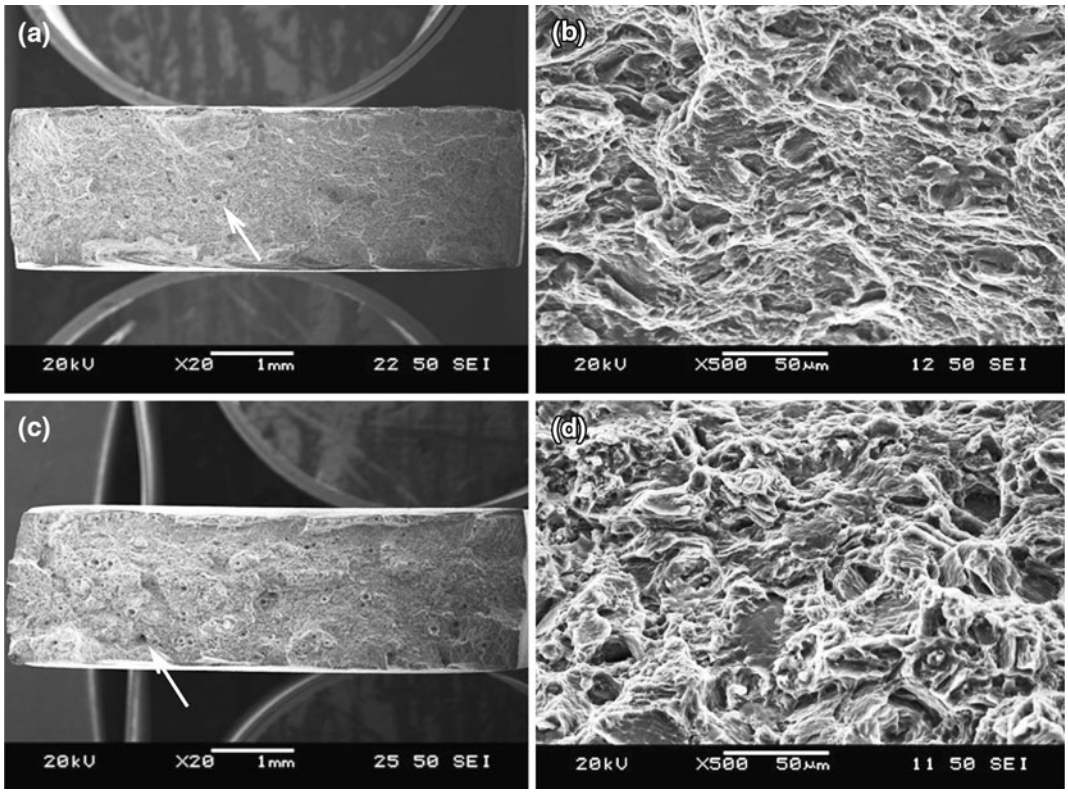

Fig. 12—Typical SEM images showing the fracture surfaces after tensile testing at a strain rate of 1×10^{-4} s^{-1}, (*a*) overall view of the entire fracture surface and (*b*) magnified view at a higher magnification of the FLW joint at a welding speed of 50 mm/s, (*c*) overall view of the entire fracture surface, and (*d*) magnified view at a higher magnification of the FLW joint at a welding speed of 100 mm/s.

with a hexagonal close-packed crystal structure was expected to also be associated with the twinning–detwinning process,[5,6] because the number of slip systems in magnesium alloys was limited at room temperature. Future studies of this aspect are needed.

IV. CONCLUSIONS

1. FLW of AZ31B-H24 Mg alloy at welding speeds of 50 mm/s and 100 mm/s led to the formation of characteristic equiaxed dendrites in the center of FZ and columnar dendrites near the FZ boundary, coupled with numerous divorced eutectic β-$Mg_{17}Al_{12}$ particles existing mainly in the interdendritic and intergranular regions, whereas recrystallized grains emerged in the HAZ. The FZ was wider, and both the dendrite cell size in the FZ and the grain size in the HAZ became larger at a welding speed of 50 mm/s as opposed to 100 mm/s. Mn-Al containing inclusions were still present in both FZ and HAZ.
2. After FLW of AZ31B-H24 Mg alloy, the lowest hardness appeared at the center of FZ. The overall hardness across the weld was slightly higher at a welding speed of 100 mm/s than that at a welding speed of 50 mm/s because of the smaller dendrite cell/grain size. Because of the narrower FZ and HAZ in the welded joint made at a welding speed of 100 mm/s, a sharper hardness profile was present.
3. Although FLW resulted in a certain reduction in the YS, ductility, and fatigue life of FLW AZ31B-H24 Mg alloy, the decrease of the UTS was moderate. A joint efficiency of about 89 pct at a welding speed of 50 mm/s and about 91 pct at a welding speed of 100 mm/s was achieved. Thus, FLW would be a favorable laser welding technique for welding Mg alloys. The hardening capacity and strain-hardening exponent increased after laser welding.

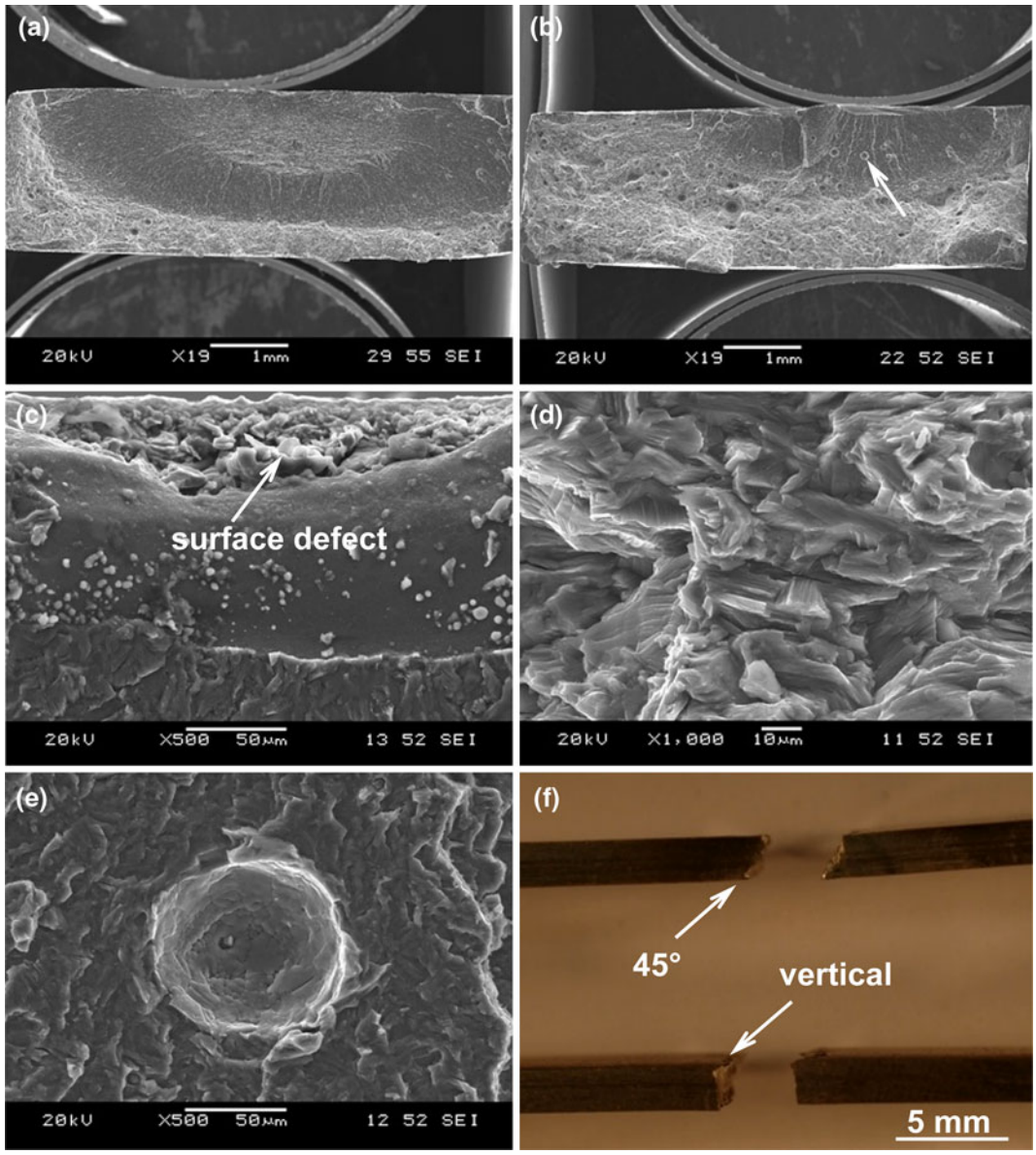

Fig. 13—Typical SEM images of fatigue fracture surface of a FLW joint at a welding speed of 50 mm/s. (*a*) Overall view of the entire fracture surface at a lower stress amplitude of 40 MPa, (*b*) multiple crack initiation at a higher stress amplitude of 80 MPa, (*c*) crack initiation site at a welding defect, (*d*) fatigue striations at a higher magnification in the propagation area, (*e*) a gas pore at a higher magnification as indicated by an arrow in (b), and (*f*) failure pattern at lower and higher stress amplitudes.

A higher welding speed led to a higher YS and longer fatigue life, but slightly lower strain-hardening exponent and hardening capacity because of the smaller grain size coupled with the eutectic structure containing β-$Mg_{17}Al_{12}$ precipitates in the FZ and smaller recrystallized grain size in the HAZ.

4. An initially higher strain-hardening rate in the BM at lower net flow stresses resulted from smaller, predeformed grains where dislocations had been generated, together with a stronger Hall–Petch contribution stemming from smaller grain sizes. At higher net flow stresses, the strain-hardening rate of the welded joints was higher, and increased more at a welding speed of 50 mm/s than at 100 mm/s, because the larger grain sizes provided more space to accommodate dislocations and increase the dislocation storage capacity during plastic deformation.
5. All tensile fracture basically occurred in the FZ, whereas fatigue failure occurred mainly between the HAZ and the FZ. Cleavage-like, flat facets together with tear ridges and river marking were observed in the welded samples. Small pores on the fracture surface of the FLW joints were observed. Fatigue crack initiated from the near-surface welding defect. At lower stress amplitudes, single crack initiation was observed, whereas multiple crack initiation was more evident at higher stress amplitudes. Fatigue crack propagation was characterized by the

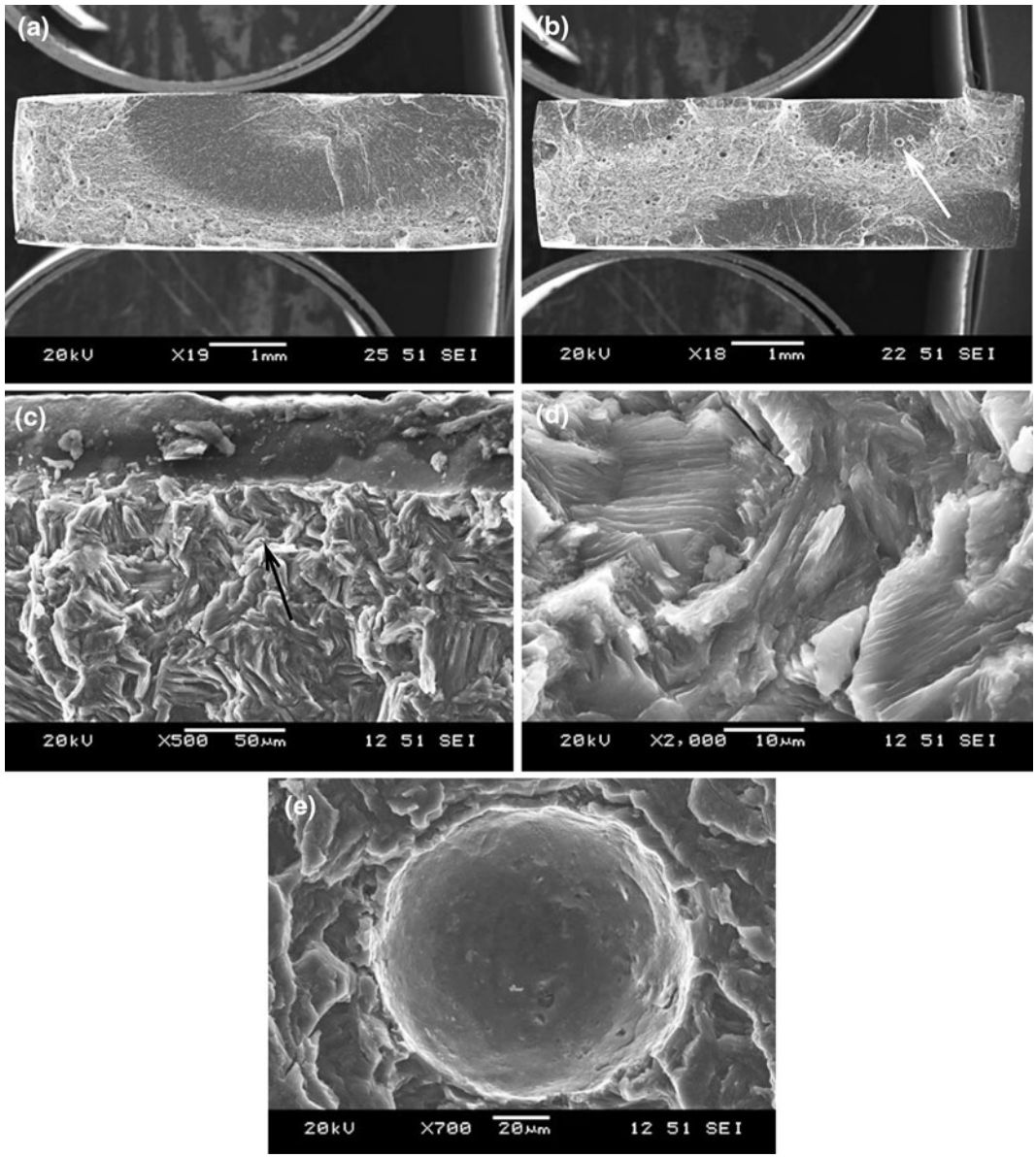

Fig. 14—Typical SEM images of fatigue fracture surface of FLW joint at a welding speed of 100 mm/s. (*a*) Overall view of the entire fracture surface at a lower stress amplitude of 40 MPa, (*b*) multiple crack initiation at a higher stress amplitude of 80 MPa, (*c*) crack initiation from a surface defect, (*d*) fatigue striations at higher a magnification in the propagation area as indicated by an arrow in (c), and (*e*) a small pore at a higher magnification as indicated by an arrow in (b).

formation of fatigue striations with increased spacing as distance increased from the initiation site in conjunction with the presence of secondary cracks.

ACKNOWLEDGMENTS

The authors would like to thank the Natural Sciences and Engineering Research Council of Canada (NSERC) and AUTO21 Network of Centers of Excellence for providing financial support. This investigation involves part of Canada-China-USA Collaborative Research Project on the Magnesium Front End Research and Development. The authors also thank General Motors Research and Development Center for supplying the test materials, and IPG Photonics Applications Lab, Novi, MI for making and supplying the fiber laser welded joints. One of the authors (D.L. Chen) is grateful for the financial support by the Premier's Research Excellence Award (PREA), NSERC-Discovery Accelerator Supplement (DAS) Award, Canada Foundation for Innovation (CFI), and Ryerson Research Chair (RRC) program. The assistance of Q. Li, A. Machin, J. Amankrah, D. Ostrom and R. Churaman (Ryerson University) in performing the experiments is gratefully acknowledged. The authors also thank Dr. X. Cao, Dr. S. Xu, Dr. K. Sadayappan, Dr. J. Jackman, Professor N. Atalla,

Professor S. Lambert, Professor H. Jahed, Professor Y.S. Yang, Professor J. Allison, Professor M.F. Horstemeyer, Professor B. Jordon, Dr. A.A. Luo, Mr. R. Osborne, Mr. J.F. Quinn, Dr. X.M. Su, and Mr. L. Zhang for their helpful discussion.

REFERENCES

1. T.M. Pollock: *Science*, 2010, vol. 328, pp. 986–87.
2. M. Wise, K. Calvin, A. Thomson, L. Clarke, B. Bond-Lamberty, R. Sands, S.J. Smith, A. Janetos, and J. Edmonds: *Science*, 2009, vol. 324, pp. 1183–86.
3. L.R. Kump: *Nature*, 2002, vol. 419, pp. 188–90.
4. W.G. Agnew: *Science*, 1974, vol. 183, pp. 254–56.
5. S. Begum, D.L. Chen, S. Xu, and A.A. Luo: *Int. J. Fatigue*, 2009, vol. 31, pp. 726–35.
6. S. Begum, D.L. Chen, S. Xu, and A.A. Luo: *Metall. Mater. Trans. A*, 2008, vol. 39A, pp. 3014–26.
7. K. Behler, J. Berkmanns, and A. Ehrhardt: *Mater. Des.*, 1997, vol. 18, p. 261.
8. E. Schubert, M. Klassen, and I. Zerner: *J. Mater. Process. Technol.*, 2001, vol. 115, p. 2.
9. X. Cao, M. Jahazi, J.P. Immarigeon, and W. Wallace: *J. Mater. Process. Technol.*, 2006, vol. 171, pp. 188–204.
10. A. Weisheit, R. Galun, and B.L. Mordike: *Weld. J.*, 1998, vol. 77, pp. 149–54.
11. H. Zhao and T. DebRoy: *Weld. J.*, 2001, vol. 80, pp. 204–10.
12. Z. Sun, D. Pan, and J. Wei: *Sci. Technol. Weld. Joining*, 2002, vol. 7, pp. 343–51.
13. L. Quintino, A. Costa, R. Miranda, D. Yapp, V. Kumar, and C.J. Kong: *Mater. Des.*, 2007, vol. 28 (4), pp. 1231–37.
14. Y. Sakai, K. Nakata, T. Tsumura, M. Ueda, T. Ueyama, and K. Akamatsu: *Mater. Sci. Forum*, 2008, vols. 580−582, pp. 479−82.
15. J. Liu, J.H. Dong, and K. Shinozaki: *Mater. Sci. Forum*, 2009, vols. 610−613, pp. 911−14.
16. L. Yu, K. Nakata, and J. Liao: *Sci. Technol. Weld. Joining*, 2009, vol. 14, pp. 554–58.
17. S.M. Chowdhury, D.L. Chen, S.D. Bhole, X. Cao, E. Powidajko, D.C. Weckman, and Y. Zhou: *Metall. Mater. Trans. A*, 2011, vol. 42A, pp. 1974–89.
18. G.F. Vander Voort: *Metallography Principles and Practice*, ASM International, Materials Park, OH, 1999.
19. ASTM Standard E8/E8M: *Standard Test Methods for Tension Testing of Metallic Materials*, ASTM International, West Conshohohocken, PA, 2008.
20. N. Afrin, D.L. Chen, X. Cao, and M. Jahazi: *Mater. Sci. Eng. A*, 2008, vol. 472, pp. 179–86.
21. L.M. Liu, G. Song, and M.L. Zhu: *Metall. Mater. Trans. A*, 2008, vol. 39, pp. 1702–11.
22. S.M. Chowdhury, D.L. Chen, S.D. Bhole, X. Cao, E. Powidajko, D.C. Weckman, and Y. Zhou: *Mater. Sci. Eng. A*, 2010, vol. 527, pp. 2951–61.
23. L. Xiao, L. Liu, D.L. Chen, S. Esmaeili, and Y. Zhou: *Mater. Sci. Eng. A*, 2011, vol. 529, pp. 81–87.
24. D. Gery, H. Long, and P. Maropoulos: *J. Mater. Process. Technol.*, 2005, vol. 167, pp. 393–401.
25. N. Kishore Babu and M. Ashfaq: *Pract. Metall.*, 2010, vol. 47 (8), pp. 426–42.
26. C.H. Fan, Z.H. Chen, W.Q. He, J.H. Chen, and D. Chen: *J. Alloys Compd.*, 2010, vol. 504 (2), pp. L42–45.
27. H.W. Wang, B. Li, J.C. Jie, and Z.J. Wei: *Mater. Des.*, 2011, in press.
28. Y.H. Xiong, A.M. Yang, P.J. Li, and L. Liu: *J. Aero. Mater.*, 2001, vol. 21 (4), pp. 5–8.
29. I. Gilath, J.M. Signamarcheix, and P. Bensussan: *J. Mater. Sci.*, 1994, vol. 29, pp. 3358–62.
30. Y.J. Quan, Z.H. Chen, X.S. Gong, and Z.H. Yu: *Mater. Charact.*, 2008, vol. 59, pp. 1491–97.
31. S. Kou: *Welding Metallurgy*, 2nd ed., Wiley, New York, NY, 2003.
32. L. Xiao, L. Liu, Y. Zhou, and S. Esmaeili: *Metall. Mater. Trans. A*, 2010, vol. 41A, pp. 1511–22.
33. M.S. Turhal and T.S. Kan: *J. Mater. Sci.*, 2003, vol. 38, pp. 2639–46.
34. M. Pareek, A. Polar, F. Rumiche, and J.E. Indacochea: *J. Mater. Eng. Perform.*, 2007, vol. 16, pp. 655–62.
35. R.C. Zeng, W. Dietzel, R. Zettler, J. Chen, and K.U. Kainer: *Trans. Nonferrous Met. Soc. China*, 2008, vol. 18, pp. S76–80.
36. G. Padmanaban, V. Balasubramanian, and J.K. Sarin Sundar: *J. Mater. Eng. Perform.*, 2010, vol. 19 (2), pp. 155–65.
37. X.Z. Lin and D.L. Chen: *J. Mater. Eng. Perform.*, 2008, vol. 17, pp. 894–901.
38. J.A. Del Valle and O.A. Ruano: *Scripta Mater.*, 2006, vol. 55, pp. 775–78.
39. S.H.C. Park, Y.S. Sato, and H. Kokawa: *Metall. Mater. Trans. A*, 2003, vol. 34A, pp. 987–94.
40. N. Afrin, D.L. Chen, X. Cao, and M. Jahazi: *Scripta Mater.*, 2007, vol. 57, pp. 1004–07.
41. W.D. Callister Jr.: *Materials Science and Engineering - An Introduction*, 8th ed., Wiley, New York, NY, 2010.
42. J. Luo, Z. Mei, W. Tian, and Z. Wang: *Mater. Sci. Eng. A*, 2006, vol. 441, pp. 282–90.
43. J.H. Hollomon: *Trans. AIME.*, 1945, vol. 162, pp. 268–89.
44. X.H. Chen and L. Lu: *Scripta Mater.*, 2007, vol. 57, pp. 133–36.
45. P. Ludwik: *Elemente der Technologischen Mechanik*, Springer-Verlag OHG, Berlin, Germany, 1909, p. 32.
46. U.F. Kocks and H. Mecking: *Progr. Mater. Sci.*, 2003, vol. 48, pp. 171–273.
47. J.A. Del Valle, F. Carreno, and O.A. Ruano: *Acta Mater*, 2006, vol. 54, pp. 4247–59.
48. C.W. Sinclair, W.J. Poole, and Y. Brechet: *Scripta Mater.*, 2006, vol. 55, pp. 739–42.
49. I. Kovacs, N.Q. Chinh, and E. Kovacs-Csetenyi: *Phys. Stat. Sol. A*, 2002, vol. 194, pp. 3–18.
50. J. Balik, P. Lukac, Z. Drozd, and R. Kuzel: *Int. J. Mater. Res.*, 2009, vol. 100 (3), pp. 322–25.
51. G.E. Dieter: *Mechanical Metallurgy*, 3rd ed., McGraw-Hill, Columbus, OH, 1986.
52. G. Padmanaban and V. Balasubramanian: *Mater. Des.*, 2010, vol. 31, pp. 3724–32.
53. L.D. Scintilla, L. Tricarico, M. Brandizzib, and A.A. Satrianoc: *J. Mater. Process. Technol.*, 2010, vol. 210, pp. 2206–14.
54. Y. Yu, C. Wang, X. Hu, J. Wang, and S. Yu: *J. Mech. Sci. Technol.*, 2010, vol. 24, pp. 1077–82.
55. K.S. Chan, Y.M. Pan, D.L. Davidson, and R.C. McClung: *Mater. Sci. Eng. A*, 1997, vol. 222, pp. 1–8.
56. C. Laird: *Fatigue Crack Propagation*, ASTM STP 415, 1967, pp. 131−68.